Journal of Materials Chemistry B

PAPER

View Article Online
View Journal | View Issue

Cite this: J. Mater. Chem. B, 2015, 3, 2455

Ca^{2+}-induced self-assembly of *Bombyx mori* silk sericin into a nanofibrous network-like protein matrix for directing controlled nucleation of hydroxylapatite nano-needles†

Mingying Yang,‡*[a] Guanshan Zhou,‡[a] Yajun Shuai,[a] Jie Wang,[a] Liangjun Zhu[a] and Chuanbin Mao*[b]

Received 24th November 2014
Accepted 27th January 2015

DOI: 10.1039/c4tb01944j

www.rsc.org/MaterialsB

Bone biomineralization is a well-regulated protein-mediated process where hydroxylapatite (HAP) crystals are nucleated with preferred orientation within the self-assembled protein matrix. Mimicking this process is a promising approach to the production of bone-like protein/mineral nanocomposites for bone repair and regeneration. Towards the goal of fabricating such nanocomposites from sericin, a protein spun by *Bombyx mori* (*B. mori*) silkworm, and bone mineral HAP, for the first time we investigated the chemical mechanism underpinning the synergistic processes of the conformational change/self-assembly of *B. mori* sericin (**BS**) as well as the nucleation of HAP on the resultant self-assembled **BS** matrix. We found that **BS**, rich in anionic amino acid residues, could bind Ca^{2+} ions from the HAP precursor solution through electrostatic attraction. The Ca^{2+} binding drove the conformational change of **BS** from random coils into β-sheets and its concomitant self-assembly into the interconnected nanofibrous network-like protein matrix, which initiated the nucleation and growth of HAP crystals. HAP crystals directed by the resultant self-assembled **BS** matrix grew preferentially along their crystallographic *c*-axis, leading to the formation of HAP nano-needles. The HAP nano-needles in the self-assembled **BS** matrix were subsequently aggregated into globules, probably driven by the hydrogen bonding between C=O groups of **BS** and O–H groups of HAP nano-needles. The present work sheds light on the chemical mechanisms of **BS** self-assembly and the controlled mineralization directed by the self-assembled matrix. We also found that the resultant nanocomposites could promote the osteogenic differentiation of human bone marrow-derived mesenchymal stem cells. Thus our work also generates a biomimetic approach to bone-like silk protein/mineral nanocomposite scaffolds that can find potential applications in bone repair and regeneration.

Introduction

In recent decades, fabrication of novel biomaterials for bone regeneration by mimicking the composition of natural bones has been a hot area in the bioengineering field. Natural bone is a hierarchically structured nanocomposite material assembled under organism's fine control. During the natural bone biomineralization, type I collagen protein self-assembles to form an organic matrix and the needle-like hydroxylapatite (HAP) nanocrystals are nucleated and oriented within the self-assembled protein matrix, generating an extracellular matrix (ECM) for supporting the growth and differentiation of bone cells.[1,2] The basic organizational unit of the ECM is mineralized type I collagen fibrils formed as a result of the oriented nucleation and growth of HAP crystals on the collagen fibrils. Inspired by bone biomineralization, using a self-assembled protein-based matrix to direct HAP formation is a promising approach to the synthesis of bone-like protein/mineral nanocomposite biomaterials for bone repair and regeneration. Therefore, choosing proteins that can not only self-assemble into a matrix but also regulate the nucleation of HAP crystals within the matrix is the key to the success of this biomimetic approach. Among all of the protein-based systems such as silks,[3,4] phages,[5–7] and collagen[8,9] being studied, silk proteins are one of the most promising candidates because silk proteins have properties desired in bone repair such as excellent biocompatibility and mechanical properties. Among silk proteins, *B. mori* sericin (**BS**), which is synthesized in the middle silk gland of *B. mori* silkworm, exhibits properties that are

[a]*Institute of Applied Bioresource Research, College of Animal Science, Zhejiang University, Yuhangtang Road 866, Hangzhou, Zhejiang 310058, China. E-mail: yangm@zju.edu.cn*

[b]*Department of Chemistry & Biochemistry, Stephenson Life Sciences Research Center, University of Oklahoma, 101 Stephenson Parkway, Norman, Oklahoma 73019-5300, USA. E-mail: cbmao@ou.edu*

† Electronic supplementary information (ESI) available. See DOI: 10.1039/c4tb01944j

‡ These two authors contributed equally to this work.

Table 1 The molar percentage of amino acids in BS

Amino acid	%
Ala	4.05
Gly	14.48
Tyr	3.39
Ser	35.63
Asp	15.65
Arg	3.10
His	1.55
Glu	4.74
Lys	2.72
Val	3.22
Leu	0.99
Ile	0.76
Phe	0.56
Pro	0.57
Thr	8.14
Met	0.14
Cys	0.29

sought in biomedical applications, such as resistance to oxidation and bacteria as well as increased hydrophilicity and biodegradation.[10–12]

BS in the form of preformed solid films or on the surface of raw silk fibers has been used as a template to grow HAP crystals.[13–17] However, these studies ignored the synergistic processes of **BS** molecular self-assembly and protein-directed HAP nucleation in solution because they used pre-formed dry solid **BS** substrates. We hypothesize that **BS** will experience conformational change and self-assembly in the presence of HAP precursor ions, which will be simultaneously coupled with the HAP nucleation to form mineralized structures. To test this hypothesis and understand the chemical mechanisms governing the synergistic process of **BS** self-assembly and HAP nucleation, this study examined the conformational change and self-assembly of **BS** as well as the HAP crystallization process initiated by incubating **BS** in an HAP precursor solution, namely, a modified simulated body fluid (1.5 SBF).

BS is a soluble protein synthesized in the silk gland of silkworm. It has abundant carboxyl groups of acidic amino acids such as Glu and Asp (Table 1). The carboxyl groups of acidic amino acids play an important role in the nucleation of HAP crystals.[18–21] The isoelectric point (pI) of **BS** is determined to be 4.1 (Fig. S1†). Hence, when **BS** is exposed to the mineralization solution buffer containing the ions of Ca^{2+} and PO_4^{3-} (Fig. 1A), we expect that the negatively charged carboxyl groups of **BS** will attract the positively charged Ca^{2+} to form a complex through electrostatic interaction, and the binding of the Ca^{2+} by **BS** will consequently trigger the conformational change of **BS** from random coils to β-sheets through hydrogen bonding and the concomitant self-assembly into a nanofibrous matrix (Fig. 1B). Our assumption is on the basis of the fact that Ca^{2+} as well as other divalent ions such as Mg^{2+} and Cu^{2+} could induce the structural transition of another silk protein, fibroin, from

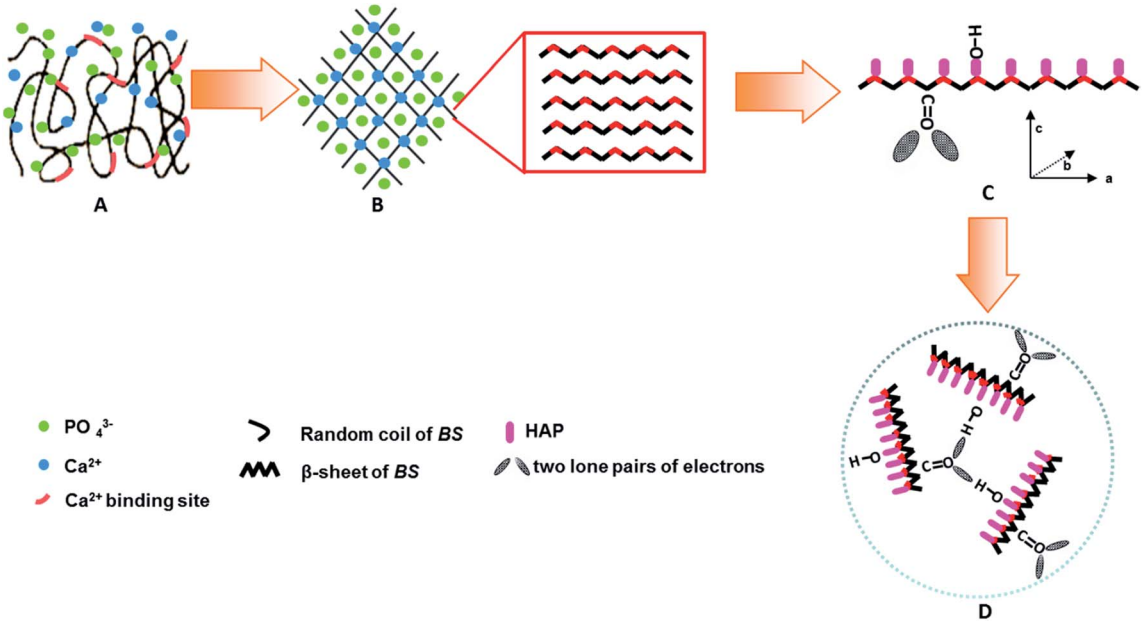

Fig. 1 Schematic illustration of BS-mediated biomineralization when BS is incubated in 1.5 SBF. (A) BS with a random coil structure is exposed to the environment containing Ca^{2+} and PO_4^{3-}, (B) Ca^{2+} binding by the anionic side-chains of BS drives the hydrogen bonding and triggers the conformational change of BS into the β-sheet structure and the concomitant self-assembly into a nanofibrous network-like matrix; (C) the nanofibrous network-like matrix with a β-sheet structure in turn initiates the nucleation of crystalline HAP nano-needles. The two lone pairs of electrons in the C=O groups of the $-COO^-$ ion of BS acted as a "proton receptor site" to attract the "proton donor site" of O–H in HAP crystals, resulting in the formation of an O–H···O hydrogen bond. It should be noted that the O–H bond in HAP crystal structure is parallel to the *c*-axis of HAP crystals.[25–27] (D) The HAP nano-needles in the self-assembled BS matrix are further assembled into globule-like clusters due to the hydrogen bonding between the C=O group in BS and the O–H group in HAP crystals. BS triggers and mediates the oriented nucleation of HAP crystals during the whole process of the mineralization.

random coils to β-sheet supports.[22–24] In turn, the Ca^{2+} ions enriched on the surface of the β-sheet structures will further attract the PO_4^{3-} from the solution buffer, initiating the preferential nucleation of the HAP crystals on the β-sheet structures and the consequent growth of HAP nuclei preferentially along their *c*-axis (*i.e.*, [001] direction) to form nano-needles (Fig. 1C). In addition, the C═O groups in the carboxyl groups in the β-sheet structures and O–H groups of HAP nuclei will interact by forming an OH···O hydrogen bond because the two lone pairs of electrons on the C═O groups can act as a "proton receptor site" to attract the "proton donor site" of the O–H groups.[25,26] Moreover, the direction of the linear O–H bond of HAP crystals will extend along the lone electron pair on the oxygen atom of the C═O groups in –COO ions to ensure that the OH···O hydrogen bond is linear (Fig. 1C and D). Since the O–H bond in HAP is parallel to the *c*-axis of the HAP crystals,[25–27] the OH···O hydrogen bonding will drive the HAP–**BS** complex to aggregate into globule structures (Fig. 1D).

To verify this hypothesis, we first investigated whether **BS** could preferentially bind to the Ca^{2+} ions due to the anionic status of the **BS** and whether such binding triggered its self-assembly into the β-sheet structures by means of circular dichroism spectroscopy (CD) and atomic force microscopy (AFM). 1.5 SBF was used as a mineralization buffer solution for **BS**-mediated HAP nucleation. **BS** was incubated in 1.5 SBF at 37.2 °C for 5 days to initiate the nucleation and growth of HAP crystals. The mineralized structures were characterized by transmission electron microscopy (TEM), X-ray diffraction (XRD) and Fourier transform infrared spectroscopy (FT-IR). Moreover, the proliferation and osteogenic differentiation of human bone marrow-derived mesenchymal stem cells (BMSCs) on both non-mineralized and mineralized **BS** were investigated.

Experimental

Preparation of aqueous BS solution

The cocoons we purchased were spun from the five-instar *B. mori* silkworms. They were dried by treating them in hot air to kill pupas inside and to remove moisture for storage. The resultant cocoons contained **BS** that are soluble in boiling water, allowing us to extract aqueous **BS** solution from cocoons at higher temperature according to the reported procedure.[28] Briefly, *B. mori* cocoons were cut into small pieces and boiled in deionized water for 10 min. This process allowed the **BS** to be dissolved in the boiling deionized water. After cooling, an aqueous **BS** solution was obtained by collecting the resultant solution followed by centrifugation. The amino acid analysis of **BS** was performed using a Hitachi L8900 Amino Acid Analyzer (Table 1). In addition, the pI of the extracted **BS** solution was calculated by measuring its zeta potential at various pH values ranging from 2.5 to 7.5.

Self-assembly of BS in the $CaCl_2$ solution

The Ca^{2+} binding ability of the aqueous **BS** solution was examined according to a previously reported method.[29] The formation rate of turbid calcium carbonate precipitates was monitored by the absorption at 570 nm of a solution prepared by adding 1.5 mL of 100 mM $CaCl_2$ solution to a mixture of 1.5 mL of 100 mM $NaHCO_3$ (pH 8.7) and 300 μL of aqueous **BS** solution with concentrations of 2.5, 5.0, 7.5 and 10.0 mg mL^{-1}. An ultraviolet spectrophotometer (SHIMADZU 2450) was used to test the absorbance at 570 nm of the resultant mixture. The Tris–HCl solution (with $NaHCO_3$ added but in the absence of **BS**) was used as a control.

To investigate the structure of **BS** in the aqueous **BS** solution, 5 mL of the aqueous **BS** solution with a concentration of 2 mg L^{-1} was incubated in 5 mL of 10 mM $CaCl_2$ overnight and then the structures formed were characterized using CD and AFM. The CD measurement was performed between 190 and 250 nm with a MOS-450 Spectrometer (Biologic, France) by diluting the concentration of **BS** to be 0.1 mg mL^{-1} in the 5 mM $CaCl_2$ solution in a 1 mm path-length cell at room temperature. Data were collected at a rate of 0.5 nm s^{-1}. Three consecutive scans were averaged and smoothed using the accompanying software program. For AFM, the concentration of the above solution was diluted to be 1×10^{-2} mg mL^{-1} with deionized water. 4 μL of this diluted solution was deposited on freshly cleaved mica and air-dried, followed by washing with 20 μL deionized water. The images were taken and processed by software (NanoScope Image). The aqueous **BS** solution was used as a control. In addition, to further investigate the effect of the concentration of $CaCl_2$ on the structural transition of **BS**, the concentration of $CaCl_2$ was varied from 1.25 to 5 mM.

Biomineralization of BS

Mineralization was performed by using the reported protocol.[2] Briefly, 1.5 SBF was first prepared by dissolving $CaCl_2$, $NaHCO_3$, KCl, $K_2HO_4 \cdot 3H_2O$, $MgCl_2$, $CaCl_2$, and Na_2SO_4 in deionized water according to the previously reported protocol.[30] The solution was then buffered at pH = 7.25 by using tris-hydroxymethyl-aminomethane or hydrochloric acid. The mineralization of **BS** was initiated by placing 10 mL of the aqueous **BS** solution into a dialysis bag and dialyzing against 1.5 SBF for up to 5 days at 37.2 °C. The resultant mineralization solution was termed **BS**/1.5SBF. The 1.5 SBF was refreshed every 12 hours.

TEM, XRD and FT-IR characterization

After mineralization for 3 and 5 days, respectively, **BS**/1.5SBF was sampled for TEM observation. To prepare samples for observation by TEM (FEI Tecnai G2F30), 10 μL of **BS**/1.5SBF was put onto a copper grid and allowed to dry. Then the sample was washed with deionized water twice to remove any soluble salts. Selected area electron diffraction (ED) was also performed. For comparison, TEM observation of non-mineralized aqueous **BS** solution was performed according to the previous report.[31] In brief, 10 μL of **BS** solution was dried on a copper grid and washed with 10 μL ddH_2O. The sample was then negatively stained with 1% uranyl acetate (UA).

In addition, **BS**/1.5SBF incubated for 5 days was freeze-dried. The obtained powder was rinsed with deionized water and then air dried. The powder was monitored by XRD (X′Pert PRO) and FT-IR (SHIMADZU 8400s). For XRD, the samples were scanned

from 10° to 60° with a scanning speed of 6° min^{-1} *in situ*. For FT-IR, the samples were pressed into discs with KBr at a mass ratio of 1 : 20. Infrared spectra were taken using a Perkin-Elmer system 2000 FT-IR spectrometer. The deconvolution of the amide I region was performed by Origin 8.5 software.

Viability and alkaline phosphatase (ALP) activity of BMSCs on BS/HAP nanocomposites

We used BMSCs as testing cells to test the proliferation and osteogenic differentiation of the cells on the **BS**/HAP nanocomposites. Cells were cultured on the samples including **BS** as well as **BS** mineralized in 1.5 SBF for 3 and 5 days (denoted as $\mathbf{BS_3}$ and $\mathbf{BS_5}$, respectively), which were coated on the culture plates, respectively. After the cells were cultured for 1, 3 and 5 days, the cell morphology was observed according to the previously reported protocol.[32] Cell Titer 96 Aqueous One Solution cell proliferation (MTS) assay was conducted to verify the cell viability according to the manufacturer's protocol (Promega). In addition, we followed our published protocols[33–35] to evaluate the osteogenic differentiation of BMSCs on **BS**, $\mathbf{BS_3}$ and $\mathbf{BS_5}$ by detecting the activity of ALP, which represents an early stage marker of the osteogenic differentiation of BMSCs.

Results and discussion

Ca^{2+} binding ability, conformational change and self-assembly of BS

In this work, we tried to obtain evidence for the Ca^{2+} binding ability of **BS** by testing its capability to inhibit the spontaneous precipitation of supersaturated $CaCO_3$.[29] Such inhibition indicated that **BS** could bind Ca^{2+} to reduce the concentration of free Ca^{2+} ions so that less $CaCO_3$ tended to precipitate from the supersaturated solution. As seen in Fig. 2A, $CaCO_3$ was prone to precipitate upon the addition of Tris–HCl solution into the supersaturated solution containing $NaHCO_3$ and $CaCl_2$ whereas the presence of **BS** in the same solution displayed a dose-dependent inhibition of $CaCO_3$ precipitation over a **BS** concentration range of 25, 5.0, 7.5 to 10.0 mg mL^{-1}, indicating the Ca^{2+} binding ability of **BS**. This proves our assumption that negatively charged carboxyl groups rich in **BS** (Table 1) can electrostatically attract the positively charged Ca^{2+}. Then the structure of Ca^{2+}-bound **BS** was investigated by the CD measurement. The aqueous **BS** solution adopted a random coil conformation in the absence of Ca^{2+}. However, addition of $CaCl_2$ solution induced the conformational change of **BS** into β-sheets overnight (Fig. 2B). We also found that the conformational change from random coils into β-sheets induced by Ca^{2+} was dependent on the concentration of $CaCl_2$ (Fig. S2†); a higher concentration is needed to achieve an obvious conformational change. It was reported that cations could induce the conformational change of another silk protein, fibroin, from random coils to β-sheets,[22–24] further proving that electrostatic attraction between negatively charged carboxyl groups rich in **BS** and positively charged Ca^{2+} can result in the conformational change of β-sheets of **BS**. AFM images further showed that the morphology of **BS** was changed from separated well-defined nano-fibrils (Fig. 2C) to interconnected nanofibrous network-like matrices (Fig. 2D) when the secondary structure of **BS** was changed from random coils to β-sheets. This morphological change was probably because hydrogen bonding interactions between **BS** nanofibers made them interconnected and aggregated to form networks. In addition, aggregation of nanofibers led to an increase in the diameter of the nanofibers in the network-like matrix (Fig. 2D). These results confirmed that Ca^{2+} binding by the acidic amino acids rich in the **BS** triggered the conformational change of **BS** from random coils to β-sheets and the concomitant self-assembly of **BS** into a nanofibrous network-like matrix that could initiate the nucleation, growth and assembly of HAP crystals.

Biomineralization of the self-assembled BS matrix

To test the formation and assembly of HAP crystals in the resultant self-assembled **BS** matrix, we incubated **BS** in 1.5 SBF at 37.2 °C for up to 5 days. TEM observation confirmed the obvious growth of HAP crystals after mineralization for 3 and 5 days (Fig. 3B–D). As a control, the structure formed in the aqueous **BS** solution (interacted with only Ca^{2+} ions but not with 1.5 SBF) was also observed by TEM (Fig. 3A). TEM imaging showed that prior to mineralization, **BS** was indeed self-assembled into a nanofibrous network-like matrix with the constituent nanofibers measuring about 10 nm in diameter (Fig. 3A). After mineralization for 3 days, nano-needles were found on the self-assembled network-like **BS** matrix (Fig. 3B). The diffraction spots from the (002) and (212) planes of HAP nano-needles in the ED pattern proved the formation of polycrystalline HAP crystals. The two white arrows in Fig. 3B highlight the fact that two populations of roughly orthogonal HAP crystals are present in the selected area. Each arrow represents the *c*-axis of one of the two HAP populations, confirming that **BS** mediates the nucleation of HAP crystals preferentially elongated along the *c*-axis. After mineralization for 5 days, HAP globules were observed (Fig. 3C). Imaging one globule at a higher magnification showed that the globule was composed of HAP nano-needles (Fig. 3D) as we expected in Fig. 1D. The ED pattern from a small area of the globule verified that the nano-needles were crystalline HAP with their long-axis being the crystallographic *c*-axis (Fig. 3D, inset).

In addition, XRD and FT-IR spectra of the mineralized self-assembled **BS** matrix proved the nucleation of HAP crystals on the matrix (Fig. 4). Two peaks at 25.8° and 32.8° in the XRD spectra (Fig. 4A) could be assigned to the (002) and (211) planes of HAP crystals, respectively, confirming that HAP crystals were nucleated on the self-assembled **BS** matrix after incubation in 1.5 SBF for 3 and 5 days. In the FT-IR spectra (Fig. 4B), the prominent peaks at 600 and 1038 cm^{-1}, which could be assigned to PO_4^{3-} v4 bending and asymmetric PO_4^{3-} v3 stretching, respectively, further confirmed the nucleation and growth of HAP crystals on the self-assembled **BS** matrix. In addition, we quantitatively determined the conformational change of **BS** by performing the deconvolution of the amide I band in the FT-IR spectra. The deconvolution results (Fig. S3

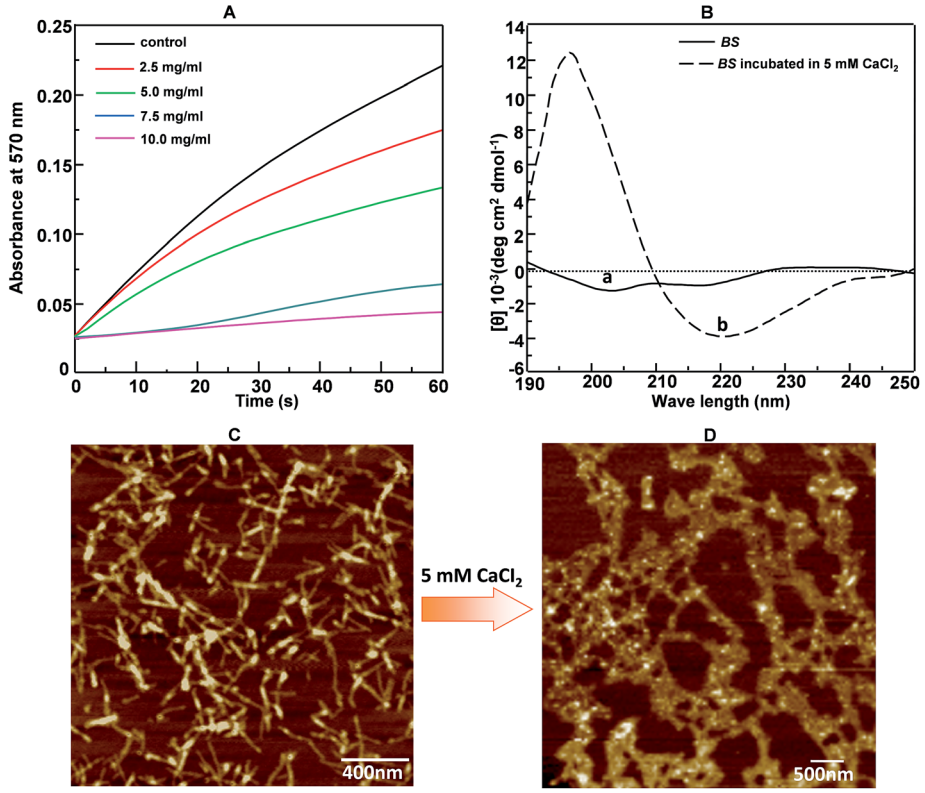

Fig. 2 Conformational change and self-assembly of **BS** in $CaCl_2$ solution. (A) The Ca^{2+} binding ability of **BS** demonstrated by the decreasing absorbance at 570 nm of the mixture (made of 1.5 mL of 100 mM $NaHCO_3$ (pH 8.7) and 300 μL of 20 mM Tris–HCl solution) in the presence of added **BS** with different concentrations (0, 2.5, 5.0, 7.5, 10.0 mg mL^{-1}) after the addition of 1.5 mL of 100 mM $CaCl_2$ (pH 8.7). The Tris–HCl solution (with $NaHCO_3$ added but in the absence of **BS**) was used as a control. The stronger inhibition of precipitation of calcium carbonate, reflected by the reduced absorbance at 570 nm due to the inhibited calcium carbonate precipitation, indicated the higher Ca^{2+} binding activity. (B) CD spectra of aqueous **BS** solution before and after the addition of 5 mM $CaCl_2$, respectively. The positive absorbance at 195 nm and negative absorbance at 217 nm indicated the appearance of the β-sheet structure. (C and D) AFM image of the protein-based structures formed in aqueous **BS** solution before (C) and (D) after pre-incubation with 10 mM $CaCl_2$ for 5 days.

and Table S1†) indicated the gradual structural transition of **BS** from random coils and β-turns to β-sheets upon mineralization.

Possible mechanism of HAP nucleation directed by the self-assembled BS matrix

BS can mediate the nucleation of HAP crystals preferentially with their long axis elongated along the *c*-axis (Fig. 3B), consistent with our speculation in Fig. 1C. After the formation of HAP nano-needles in the self-assembled **BS** matrix, **BS** and HAP crystals in the mineralized matrix can form hydrogen bonding by the interaction between the two lone pairs of electrons of C=O of **BS** and the OH of HAP nano-needles (Fig. 1C).[25–27] Such a hydrogen bonding interaction is expected to force HAP nano-needles to be clustered into a globule-like structure (Fig. 1D). This hypothesis was further confirmed by the fact that HAP globules were indeed observed after mineralization for 5 days (Fig. 3C). Moreover, the broadening of the O–H band as well as the shift of the O–H band to a lower wavenumber (Fig. 5) is direct evidence for the formation of hydrogen bonding (HO···H) between OH in HAP and the C=O group in **BS** with the β-structure as predicted in Fig. 1. Collectively, the data from AFM and TEM images as well as XRD and FT-IR spectra all confirm our hypothesis on the **BS**-templated biomineralization proposed in Fig. 1. Namely, Ca^{2+} ions in the HAP precursor solution (1.5 SBF) trigger the conformational change of **BS** from random coils to β-sheets and the concomitant self-assembly of **BS** into nanofibrous network-like matrices. Then the Ca^{2+}-bearing self-assembled **BS** matrix electrostatically attracts PO_4^{3-} to cause the super-saturation of HAP on the surface of the matrix and consequently initiates the nucleation of HAP nano-needles. Finally, the hydrogen bonding interaction between the C=O groups of **BS** and OH groups (parallel to the *c*-axis of HAP crystals) of HAP nano-needles drives the assembly of HAP nano-needles into globules.

Cell proliferation and differentiation on BS/HAP nanocomposites

To determine that HAP crystals can improve the proliferation and osteogenic differentiation of BMSCs on the **BS**-based materials, we seeded BMSCs on a non-mineralized **BS** matrix as well as **BS**/HAP nanocomposites including $\mathbf{BS_3}$ and $\mathbf{BS_5}$, then examined the cell morphology by immunofluorescence (Fig. 6A), cell proliferation by MTS assay (Fig. 6B) and osteogenic differentiation by ALP activity assay (Fig. 6C). The

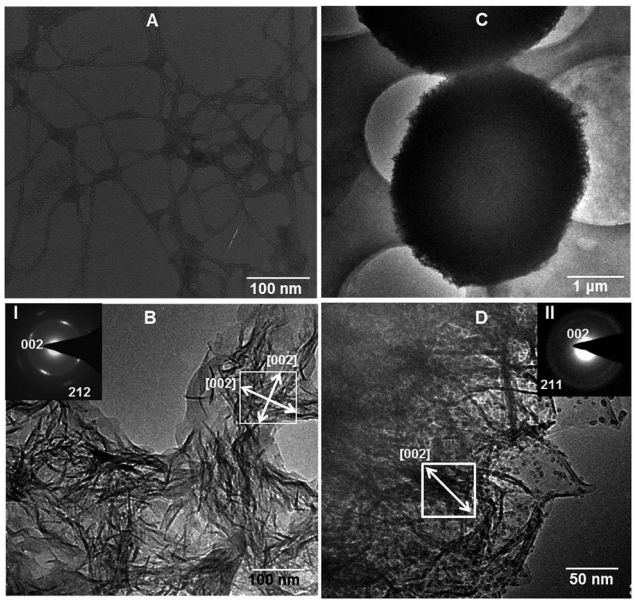

Fig. 3 TEM images of **BS** before (A, only interacted with Ca^{2+}) and after (B–D) mineralized in 1.5 SBF at 37.2 °C for 3 days (B) and 5 days (C and D). D is the high magnification image corresponding to (C). Insets in (B and D) (I and II) are electron diffraction patterns taken from the area highlighted by a white square in (B and D), respectively. White arrows indicate the [002] direction (*i.e.*, the *c*-axis direction) of the HAP crystals.

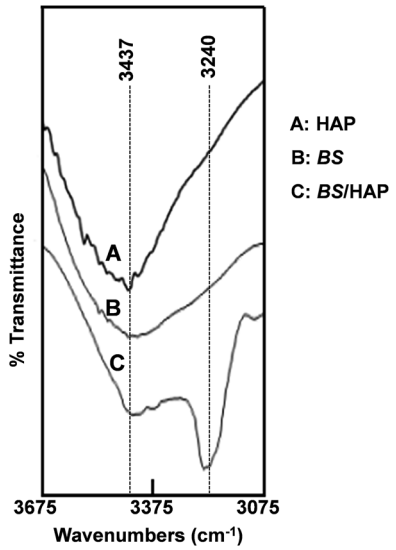

Fig. 5 FTIR spectra of O–H stretching vibrations of synthetic HAP crystals (A), **BS** (B), and **BS**/HAP (C). The O–H peak is shifted to a smaller wavenumber and becomes broader as a result of the hydrogen bonding between HAP and **BS** as predicted in Fig. 1C.

confocal micrographs indicated that cells spread widely on the $\mathbf{BS_3}$ and $\mathbf{BS_5}$ compared to those on the **BS**. This result illustrated that **BS**/HAP nanocomposites could support cell adhesion and spreading. After being cultured for 5 days, the cells exhibited a more stellate-patterned phenotype on $\mathbf{BS_3}$ and $\mathbf{BS_5}$, and more cells were observed on the $\mathbf{BS_5}$ than the **BS**. MTS assay further confirmed that the proliferation rate on $\mathbf{BS_3}$ and $\mathbf{BS_5}$ was higher than on **BS**, and $\mathbf{BS_5}$ shows a higher proliferation rate than $\mathbf{BS_3}$ (Fig. 6B). In addition, ALP assay (Fig. 6C) showed that the ALP activity of BMSCs on both $\mathbf{BS_3}$ and $\mathbf{BS_5}$ was significantly higher than the **BS** ($p < 0.01$), suggesting that **BS**/HAP nanocomposites promoted the early stage of osteogenic differentiation of BMSCs in comparison with **BS** without HAP crystals. Furthermore, it indicated that $\mathbf{BS_5}$ had a higher capacity in promoting the osteogenic differentiation than $\mathbf{BS_3}$. Therefore, the MTS assay and ALP assay results indicated that HAP crystals can promote the proliferation and osteogenic differentiation of BMSCs, and increasing mineralization time

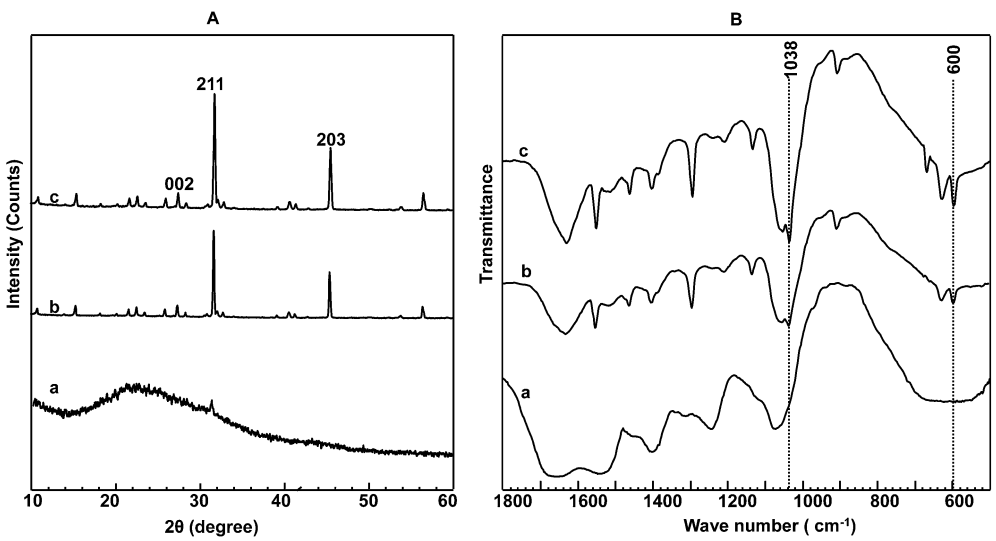

Fig. 4 (A) XRD patterns and (B) FT-IR spectra of **BS** before (a, only interacted with Ca^{2+}) and after being mineralized for different times (b, 3 days; c, 5 days). The appearance of the (203), (211) and (002) planes proved the nucleation of HAP crystals on the self-assembled **BS** matrix. The prominent peaks at 600 and 1038 cm^{-1} in B indicated the formation of HAP crystals on the **BS**.

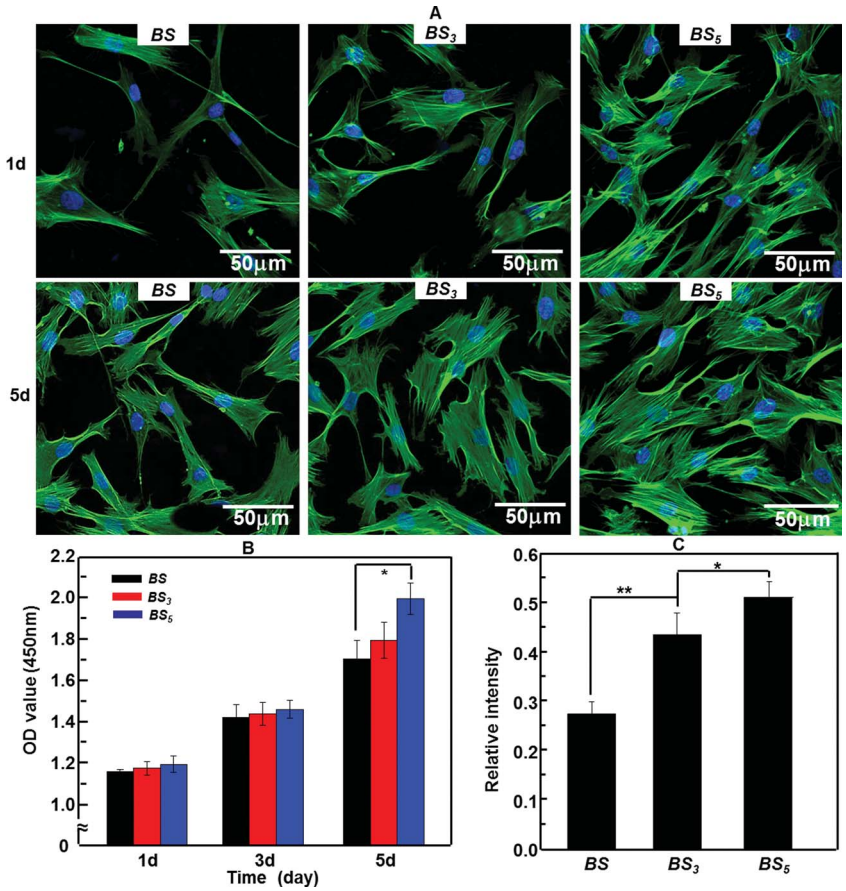

Fig. 6 (A) Morphology of human BMSCs on **BS**, BS_3, and BS_5 with actin stained in green and nuclei stained in blue by DAPI after being cultured for 1 day and 5 days. BMSCs were adherent more strongly and proliferated faster on BS_5. (B) MTS assay of BMSC proliferation on **BS**, BS_3 and BS_5 after being cultured for 1 day, 3 days and 5 days. (C) Assay of the enzymatic activity of the early osteogenic differentiation marker, alkaline phosphatase (ALP), showing that BS_3 and BS_5 promoted the osteogenic differentiation of BMSCs in comparison to the **BS**. In addition, BS_5 shows better capability in promoting the osteogenic differentiation of BMSCs than the BS_3.*$p < 0.05$, **$p < 0.01$. **BS**, BS_3, and BS_5 denote *B. mori* sericin, and *B. mori* sericin mineralized for 3 days and 5 days, respectively.

can also promote the cell proliferation and osteogenic differentiation. The promotion of the osteogenic capacity of biomolecular materials by HAP was in agreement with our recent findings.[32,36] It suggested that **BS**/HAP nanocomposites can be used as a biocompatible and osteogenic biomaterial for bone regeneration and repair.

Conclusion

To gain an understanding of the synergetic process of **BS** self-assembly and HAP nucleation as well as the chemical mechanism of **BS**-templated biomineralization, we have studied how **BS** undergoes the conformational change and self-assembly process in the presence of HAP precursor ions, and then initiates the nucleation and assembly of HAP nano-needles. For the first time, we find that Ca^{2+} ions in the HAP precursor solution can trigger the conformational change of **BS** from random coils into β-sheets and the concomitant self-assembly from separated nanofibers into the interconnected nanofibrous network-like matrix. The self-assembled **BS** matrix then induces the nucleation of HAP nano-needles with their long axis along the *c*-axis in the presence of PO_4^{3-} ions. Due to the hydrogen bonding interaction between the C=O of **BS** and O–H groups of HAP nano-needles, the HAP nano-needles are forced to assemble into globules. These assembled **BS**/HAP globules significantly promote the proliferation and osteogenic differentiation of BMSCs when compared to the non-mineralized **BS**. Thus the mineralized self-assembled **BS** matrix can mimic the mineralized self-assembled collagen matrix in natural bone to some extent and thus potentially serve as building blocks for the development of biocompatible protein/mineral scaffolds to support the growth and differentiation of stem cells for bone repair and regeneration.

Acknowledgements

M.Y. acknowledges the support of Zhejiang Provincial Natural Science Foundation of China (LZ12C17001) and Projects of Zhejiang Provincial Science and Technology Plans (2012C12910), National Natural Science Foundation of China (21172194), Silkworm Industry Science and Technology Innovation Team (2011R50028), National High Technology Research

and Development Program 863 (2013AA102507). CBM would like to thank the financial support from National Institutes of Health (EB015190), National Science Foundation (DMR-0847758, CMMI-1234957 and CBET-0854414), Department of Defense Peer Reviewed Medical Research Program (W81XWH-12-1-0384), Oklahoma Center for Adult Stem Cell Research (434003) and Oklahoma Center for the Advancement of Science and Technology (HR14-160).

Notes and references

1 S. Weiner and H. D. Wagner, *Annu. Rev. Mater. Sci.*, 1998, **28**, 271–298.
2 F. Nudelman, K. Pieterse, A. George, P. H. Bomans, H. Friedrich, L. J. Brylka, P. A. Hilbers, G. de With and N. A. Sommerdijk, *Nat. Mater.*, 2010, **9**, 1004–1009.
3 M. Y. Yang, W. He, Y. J. Shuai, S. J. Min and L. J. Zhu, *J. Polym. Sci., Part B: Polym. Phys.*, 2013, **51**, 742–748.
4 T. Furuzono, T. Taguchi, A. Kishida, M. Akashi and Y. Tamada, *J. Biomed. Mater. Res.*, 2000, **50**, 344–352.
5 F. Wang, B. Cao and C. B. Mao, *Chem. Mater.*, 2010, **22**, 3630–3636.
6 T. He, G. Abbineni, B. Cao and C. B. Mao, *Small*, 2010, **6**, 2230–2235.
7 H. Xu, B. Cao, A. George and C. Mao, *Biomacromolecules*, 2011, **12**, 2193–2199.
8 A. S. Deshpande and E. Beniash, *Cryst. Growth Des.*, 2008, **8**, 3084–3090.
9 Y. Wang, C. Yang, X. Chen and N. Zhao, *Adv. Eng. Mater.*, 2006, **8**, 97–100.
10 A. Nishida, T. Naganuma, T. Kanazawa, Y. Takashima, M. Yamada and H. Okada, *Int. J. Pharm.*, 2011, **407**, 44–52.
11 Y. Zhang, *Biotechnol. Adv.*, 2002, **20**, 91–100.
12 S. Nayak, S. Talukdar and S. Kundu, *Cell Tissue Res.*, 2012, **347**, 783–794.
13 A. Takeuchi, C. Ohtsuki, T. Miyazaki, M. Kamitakahara, S. Ogata, M. Yamazaki, Y. Furutani, H. Kinoshita and M. Tanihara, *J. R. Soc., Interface*, 2005, **2**, 373–378.
14 A. Takeuchi, C. Ohtsuki, M. Kamitakahara, S. Ogata, M. Tanihara, T. Miyazaki, M. Yamazaki, Y. Furutani and H. Kinoshita, *Key Eng. Mater.*, 2004, **254**, 403–406.
15 M. Yang, N. Mandal, Y. Shuai, G. Zhou, S. Min and L. Zhu, *Bio-Med. Mater. Eng.*, 2014, **24**, 815–824.
16 Y. Cai, J. Jin, D. Mei, N. Xia and J. Yao, *J. Mater. Chem.*, 2009, **19**, 5751–5758.
17 Y. Cai, D. Mei, T. Jiang and J. Yao, *Mater. Lett.*, 2010, **64**, 2676–2678.
18 A. George and A. Veis, *Chem. Rev.*, 2008, **108**, 4670–4693.
19 A. George, L. Bannon, B. Sabsay, J. W. Dillon, J. Malone, A. Veis, N. A. Jenkins, D. J. Gilbert and N. G. Copeland, *J. Biol. Chem.*, 1996, **271**, 32869–32873.
20 G. He, T. Dahl, A. Veis and A. George, *Nat. Mater.*, 2003, **2**, 552–558.
21 G. He, T. Dahl, A. Veis and A. George, *Connect. Tissue Res.*, 2003, **44**, 240–245.
22 A. Ochi, K. S. Hossain, J. Magoshi and N. Nemoto, *Biomacromolecules*, 2002, **3**, 1187–1196.
23 L. Zhou, X. Chen, Z. Shao, P. Zhou, D. P. Knight and F. Vollrath, *FEBS Lett.*, 2003, **554**, 337–341.
24 X. H. Zong, P. Zhou, Z. Z. Shao, S. M. Chen, X. Chen, B. W. Hu, F. Deng and W. H. Yao, *Biochemistry*, 2004, **43**, 11932–11941.
25 C. B. Mao, H. Li, F. Cui, C. Ma and Q. Feng, *J. Cryst. Growth*, 1999, **206**, 308–321.
26 C. B. Mao, H. Li, F. Cui, Q. Feng and C. Ma, *J. Mater. Chem.*, 1999, **9**, 2573–2582.
27 B. Cao and C. B. Mao, *Langmuir*, 2007, **23**, 10701–10705.
28 H. Zhang, L. Deng, M. Yang, S. Min, L. Yang and L. Zhu, *Int. J. Mol. Sci.*, 2011, **12**, 3170–3181.
29 M. Yang, T. Muto, D. Knight, A. M. Collins and T. Asakura, *Biomacromolecules*, 2008, **9**, 416–420.
30 A. Takeuchi, C. Ohtsuki, T. Miyazaki, H. Tanaka, M. Yamazaki and M. Tanihara, *J. Biomed. Mater. Res., Part A*, 2003, **65**, 283–289.
31 B. Cao, H. Xu and C. Mao, *Microsc. Res. Tech.*, 2011, **74**, 627–635.
32 M. Yang, Y. Shuai, C. Zhang, Y. Chen, L. Zhu, C. Mao and H. OuYang, *Biomacromolecules*, 2014, **15**, 1185–1193.
33 J. Wang, L. Wang, X. Li and C. Mao, *Sci. Rep.*, 2013, **3**, 1242.
34 H. Zhu, B. Cao, Z. Zhen, A. A. Laxmi, D. Li, S. Liu and C. B. Mao, *Biomaterials*, 2011, **32**, 4744–4752.
35 L. Hao, H. Yang, C. Du, X. Fu, N. Zhao, S. Xu, F. Cui, C. B. Mao and Y. Wang, *J. Mater. Chem. B*, 2014, **2**, 4794–4801.
36 M. Yang, G. Zhou, H. Castano, Y. Zhu and C. B. Mao, *J. Biomed. Nanotechnol.*, 2015, **11**, 447–456.

